

## Research Article

# Doped Nanostructured Manganese Ferrites: Synthesis, Characterization, and Magnetic Properties

Sami-ullah Rather<sup>ID</sup>,<sup>1</sup> Usman Saeed,<sup>1</sup> Abdulrahim Ahmad Al-Zahrani,<sup>1</sup> Hisham S. Bamufleh,<sup>1</sup> Hesham Abdulhamed Alhumade,<sup>1</sup> Aqeel Ahmad Taimoor,<sup>1</sup> O. M. Lemine,<sup>2</sup> Arshid Mahmood Ali,<sup>1</sup> Belal Al Zaitone,<sup>1</sup> and Muhammad Mahmud Alam<sup>1</sup>

<sup>1</sup>Department of Chemical and Materials Engineering, King Abdulaziz University, P.O. Box 80204 Jeddah 21589, Saudi Arabia

<sup>2</sup>Physics Department, College of Sciences, Imam Mohammad Ibn Saud Islamic University (IMSIU), Riyadh, Saudi Arabia

Correspondence should be addressed to Sami-ullah Rather; rathersami@kau.edu.sa

Received 23 August 2021; Revised 24 November 2021; Accepted 30 November 2021; Published 24 December 2021

Academic Editor: Filippo Giubileo

Copyright © 2021 Sami-ullah Rather et al. This is an open access article distributed under the Creative Commons Attribution License, which permits unrestricted use, distribution, and reproduction in any medium, provided the original work is properly cited.

Nanocrystalline aluminum-doped manganese ferrite was synthesized by facile thermal treatment method. Nanostructure-doped ferrite with crystalline size that ranged between 3.71 and 6.35 nm was characterized via X-ray diffraction (XRD), scanning electron microscopy (SEM), X-ray photoelectron spectroscopy (XPS), and vibrating-sample magnetometry (VSM). The Scherrer and Williamson-Hall hypothesis techniques were utilized to determine lattice constants and strain. Various types of structural properties including octahedral and tetrahedral site radius, bond lengths and angles, hopping parameter, oxygen positional parameters, site bonds, and edge lengths were determined from XRD spectrum analysis. Discrepancy in the hypothetically expected angle indicates improvement of A-B superexchange intercommunication. Furthermore, magnetic-hysteresis (M-H) and XPS analysis support the claim of enhancement. The presence of the ionic nature of iron and manganese in ferrite is Fe<sup>II</sup>, Fe<sup>III</sup>, Mn<sup>II</sup>, and Mn<sup>IV</sup> as revealed by the results of XPS. Moreover, XPS assists in an excellent way to understand the properties such as configuration, chemical nature, and average inversion degree of doped ferrite samples. The spin noncollinearity and exquisite interaction amid the sublattice are responsible for the decrease in the saturation and remnant magnetization determined from the hysteresis loop at ambient temperature with maximum magnetic field of 1.8 T.

## 1. Introduction

The transition metal-oriented nanoferrites which consist of unique structural, electrical, thermal, and magnetic characteristics are utilized for various types of engineering and biomedical applications. Nanostructure ferrites are used in different types of biological applications such as X-ray diagnosis, drug delivery, hyperthermia, and magnetic resonance imaging (MRI) [1–4]. Moreover, nanocrystalline spinel ferrites possess a variety of characteristics which are applied in the field of electromagnetic interference (EMI), circuit-based electronic, pigments, sensors, radar systems, motors, and inductors [5–12]. Manganese ferrite ( $MnFe_2O_4$ ) nanoparticles (NPs) with other ferrites are considered as a crucial tool for biomedical applications particularly for enhancing

efficiency of magnetic resonance imaging, hyperthermia, and drug delivery [13]. The properties such as facile preparation, proper saturation magnetization, inflated Curie temperature, high coercivity, and redundant anisotropic constant make manganese NPs an exceptional contender for biological applications [14, 15].

Generally spinel-based ferrites are represented by the specification  $AB_2O_4$ , where A and B indicates divalent and trivalent cations. Ferrites exhibit different types of unit cell with eight formula units in each cell. The oxygen anions with larger size and metal cations with smaller size occupies face-centered cubic (fcc) and interstitial sites, respectively. The magnetite ( $Fe_3O_4$ ), a form of iron oxide is the primary building block of most of the ferrites [16]. The  $(M^{2+})_{1-\delta}Fe^{3+}_{\delta}[M^{2+}_{\delta}Fe^{3+}_{2-\delta}]O_4$  formula provides general information

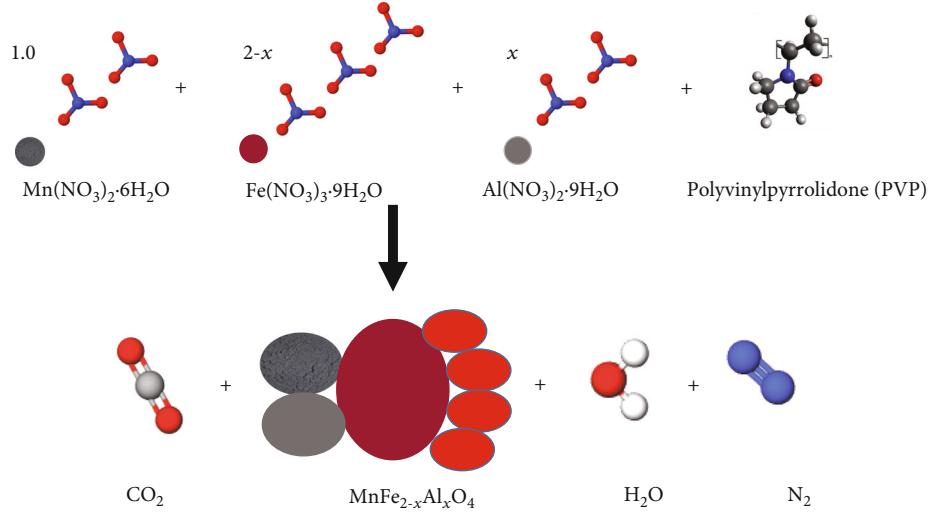


FIGURE 1: Schematic design of the reaction arrangement of the synthesis of  $\text{MnFe}_{2-x}\text{Al}_x\text{O}_4$ .

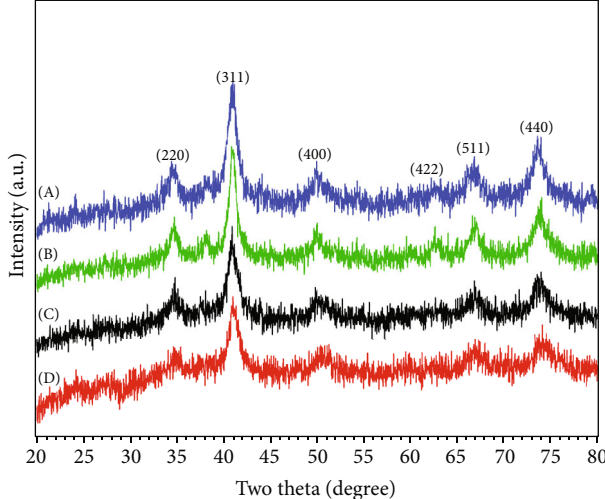


FIGURE 2: XRD patterns of  $\text{MnFe}_{2-x}\text{Al}_x\text{O}_4$ . Profiles a, b, c, and d refer to Al content of  $x = 0.0, 0.3, 0.6$ , and  $0.9$ , respectively.

related to sites and degree of inversion ( $\delta$ ). The () and [] bracket represents tetrahedral and octahedral sections and “ $\delta$ ” furnishes ferrite nature in terms of whether the structure is normal, inverse or random. When  $\delta = 0$ , the formula is expressed as  $(\text{M}^{2+})[\text{Fe}_2^{3+}\text{O}_4]$ , and the ferrite is called normal spinel ferrite. When  $\delta = 1$ , the formula is expressed as  $(\text{Fe}^{3+})[\text{M}^{2+}\text{Fe}^{3+}\text{O}_4]$ , and the ferrite is called inverse spinel ferrite. When  $0 < \delta < 1$ , such as  $\delta = 0.3, 0.6$ , or  $0.9$ , the ferrite is called as mixed spinel ferrite. When  $\delta = 0.3$ , the formula is expressed as  $(\text{M}_{0.7}^{2+}\text{Fe}_{0.3}^{3+})[\text{M}_{0.3}^{2+}\text{Fe}_{1.7}^{3+}\text{O}_4]^{2-}$  [17]. Zinc ferrite ( $\text{ZnFe}_2\text{O}_4$ ), a normal spinel, where  $\text{Zn}^{2+}$  cations represent as tetrahedral site and  $\text{Fe}^{3+}$  cations as octahedral sites leads to the formula as  $(\text{Zn}^{2+})[\text{Fe}_2^{3+}\text{O}_4]$  [18]. Cobalt ferrite ( $\text{CoFe}_2\text{O}_4$ ) is an inverse ferrite, where  $\text{Co}^{2+}$  prefers octahedral and  $\text{Fe}^{3+}$  prefers uniform placement in octahedral and tetrahedral sites [19]. Manganese ferrite ( $\text{MnFe}_2\text{O}_4$ ) is a mixed ferrite, where  $\text{Mn}^{2+}$  and  $\text{Fe}^{3+}$  prefer both tetrahedral and octahedral bonding sites [20]. Structural, magnetic,

and optical characteristics of ferrites depends upon tetrahedral and octahedral sites occupied by divalent and trivalent cations [21, 22]. Furthermore, particle size distribution (PSD) also affects optical and magnetic characteristics of spinel ferrites [23, 24].

Ferrite nanoparticles bearing new unique characteristics are prepared by different routes which include high-energy ball milling, solvothermal, coprecipitation, sol-gel method, thermal decomposition, hydrothermal, microemulsion, electrochemical, and laser ablation method [25–33]. It was reported that the crystal structure, size, and magnetic properties of ferrites including manganese ferrite are influenced by calcinations, reaction duration, capping reagent, and pH [34–36]. The preparation methods including thermal decomposition, microemulsion, and coprecipitation affect crystal structure and magnetic properties of ferrites as reported by Gyergyek et al. [37]. Furthermore, it was also reported that different types of the preparation method change cation distribution, composition, and crystallinity among tetrahedral and octahedral sites [37–39]. The lattice parameter and average strain of cobalt ferrites vary with doping of erbium. Furthermore, this variation is due to a large size of  $\text{Er}^{3+}$  cations as compared to  $\text{Fe}^{3+}$  ions [40]. Incorporation of Mg into  $\text{ZnFe}_2\text{O}_4$  significantly affects the rearrangement of cation distribution at tetrahedral and octahedral sites [41]. The crystal size of nickel-cobalt spinel changes upon doping of rare-earth metals. Moreover, variation in crystal size is because of blocking of crystal expansion by large size metals. The crystal size and surface area of ferrite are influenced by changing the variation of different types of metals such as La, Zn, Cd, and Ni [27, 40–44].

In this research work, the preparation of mixed spinel ferrite  $\text{MnFe}_{2-x}\text{Al}_x\text{O}_4$  ( $0 \leq x \leq 0.9$ ) with  $(x) = 0.0, 0.3, 0.6$ , and  $0.9$  via a thermal method in association with capping agent polyvinylpyrrolidone is presented in detail. For mixed doped manganese spinel ferrite preparation, thermal disintegration route was chosen because of distinct accomplishments such as environmental acceptance, cheap, and

TABLE 1: XRD parameters of  $\text{MnFe}_{2-x}\text{Al}_x\text{O}_4$  ( $x = 0.0, 0.3, 0.6$ , and  $0.9$ ).

Sample name	Lattice parameter $a$ (Å)	Cell volume $V$ (Å) <sup>3</sup>	Bulk density $\rho_m$ (gm/ cm <sup>3</sup> )	X-ray density $\rho_{x\text{-ray}}$ (gm/ cm <sup>3</sup> )	Porosity (%)	Crystal size (nm)
$\text{MnFe}_2\text{O}_4$	8.515	617.380	2.998	4.962	39.580	6.35
$\text{MnAl}_{0.3}\text{Fe}_{1.7}\text{O}_4$	8.512	613.910	2.885	4.775	39.581	5.99
$\text{MnAl}_{0.6}\text{Fe}_{1.4}\text{O}_4$	8.499	605.170	2.772	4.589	39.583	4.47
$\text{MnAl}_{0.9}\text{Fe}_{1.1}\text{O}_4$	8.458	601.120	2.660	4.403	39.586	3.71

persistent reproducibility; however, this process has a few drawbacks which include shape discrepancy and cluster of particles. Detailed characterization analysis of crystal structural parameter, nanostructure morphology, and quantitative assessment and magnetization characteristics of purified and Al-doped manganese mixed ferrite were also reported in this research work.

## 2. Experimental

**2.1. Synthesis.** Analytical precursors were used for the synthesis of pure and Al-doped manganese ferrite  $\text{MnFe}_{2-x}\text{Al}_x\text{O}_4$  ( $x = 0.0, 0.3, 0.6$ , and  $0.9$ ) without repeating purification: polyvinylpyrrolidone (PVP) (Alfa Aesar), iron (III) nitrate nonahydrate  $[\text{Fe}(\text{NO}_3)_3 \cdot 9\text{H}_2\text{O}]$  (min. 98%, Sigma-Aldrich), manganese (II) nitrate hexahydrate  $[\text{Mn}(\text{NO}_3)_2 \cdot 6\text{H}_2\text{O}]$  (min. 98%, Sigma-Aldrich), and aluminum nitrate nonahydrate  $[\text{Al}(\text{NO}_3)_3 \cdot 9\text{H}_2\text{O}]$  (min. 98%, Sigma-Aldrich).

In a thermal synthesis process of  $\text{MnFe}_2\text{O}_4$ , a solution containing 0.2 mmol (0.0808 g)  $\text{Fe}(\text{NO}_3)_3 \cdot 9\text{H}_2\text{O}$  and 0.1 mmol (0.0179 g)  $\text{Mn}(\text{NO}_3)_2 \cdot 6\text{H}_2\text{O}$  was vigorously stirred for 2 h, followed by inclusion of capping agent (PVP) solution. The capping agent solution was synthesized by adding 0.1 g of PVP into 50 ml of deionized water (DI) at 90°C. The mixed solution was vigorously stirred for 2 h at room temperature (RT). The pH of the above solution was determined by litmus paper which was followed by drying at 80°C for 24 h. The dried orange-colored sample was converted into powder and calcinated at 500°C for 4 h to eliminated PVP in order to form pristine  $\text{MnFe}_2\text{O}_4$ . A similar method was executed for the preparation of  $\text{MnFe}_{2-x}\text{Al}_x\text{O}_4$  ( $x = 0.3, 0.6$ , and  $0.9$ ). For clarity, hereafter, the Al-doped  $\text{MnFe}_2\text{O}_4$  are referred to as  $\text{MnFe}_{1.7}\text{Al}_{0.3}\text{O}_4$ ,  $\text{MnFe}_{1.4}\text{Al}_{0.6}\text{O}_4$ , and  $\text{MnFe}_{1.1}\text{Al}_{0.9}\text{O}_4$ . A graphic reaction design for the synthesis of  $\text{MnFe}_{2-x}\text{Al}_x\text{O}_4$  is presented in Figure 1.

**2.2. Characterization.** Structure of pristine and doped ferrite was determined by the XRD spectrum. The XRD spectrum was achieved using an INEL CPS 180 XRD Equinox 1000 diffractometer assembled with Co-K $\alpha 1$  emission ( $\lambda = 1.789$  Å) and regulated at 40 kV and 30 mA. The analysis was managed in the  $2\theta$  range of 10-80° at RT. The nanostructure behavior of samples was investigated by SEM. A wafer-delicate carbon film captivated inner side of a copper framework was used to install nanoparticles present in an ethanol solution. The XPS was operated by employing the SPEC GmbH (Germany) spectrometer at RT. The instrument is assembled with X-ray-bearing dual anode origin

SPECS XR-50 Mg-K $\alpha$  ( $h\nu = 1283.6$  eV) in the presence of lift-off angle of photoelectrons of 90°. The ferrite samples were converted into pellets, before shifting to a high vacuum chamber. The vacuum was managed at  $5 \times 10^{-9}$  bar, during the operation. In order to perform surface quantification of the ferrite sample, a detailed operating method was employed containing high-resolution spectrum of O1s and C1s. To achieve a high quality XPS spectrum, calibration of the BE scale was performed by BE of C1s peak at 284.6 eV. The Lake Shore 7400 magnetometer VSM that was equipped with a 1.8 Tesla magnet was utilized to determine magnetic properties of ferrite samples at RT. The hysteresis loop of ferrite samples was obtained by plotting magnetization versus magnetic field. Furthermore, to measure remnant magnetization (Mr), saturation magnetization (Ms), and coercivity, magnetic hysteresis loops were utilized.

## 3. Results and Discussion

Powder XRD pattern results of  $\text{MnFe}_{2-x}\text{Al}_x\text{O}_4$  ( $0 \leq x \leq 0.9$ ) are presented in Figure 2, and profiles a, b, c, and d refer to the content of  $x = 0.0, 0.3, 0.6$  and  $0.9$ , respectively. The visibly strong peaks were found between 10 and 80°. The strong peaks shown in Figure 2 are contemplations from the (111), (220), (311), (222), (400), (422), (511), (440), (620), (533), and (444) planes of purified and Al-doped ferrites. All these prominent peaks are associated to Bragg's contemplation of cubic ferrite with space group Fd3m. The nonexistence of other oxide peaks suggests that precursor is free from impurity. The inflation of Al content produces broadened diffraction peaks and simultaneously decreases intensity, which indicates development of nanostructured ferrites. The strong main peak (311) refers to crystallinity of the structure of ferrites. The decrease in crystallite size as the Al content elevates is shown in Table 1. The full width at half-maximum is utilized in the Scherer equation (Equation (1)) to determine crystal size (D). The main peak in the XRD spectrum was employed to calculate crystal size.

$$D = \frac{(0.9 \lambda)}{(\beta_{hkl} \cos\theta)}. \quad (1)$$

X-ray wavelength, FWHM in radians, and Bragg's angle, respectively, refer to  $\lambda$ ,  $\beta$ , and  $\theta$ .

Table 1 shows average crystal size data calculated from Equation (1) and was found to be 6.35, 5.99, 4.47, and 3.71 nm. The capping agent PVP was employed during the synthesis process to avert agglomeration of ferrite particles.

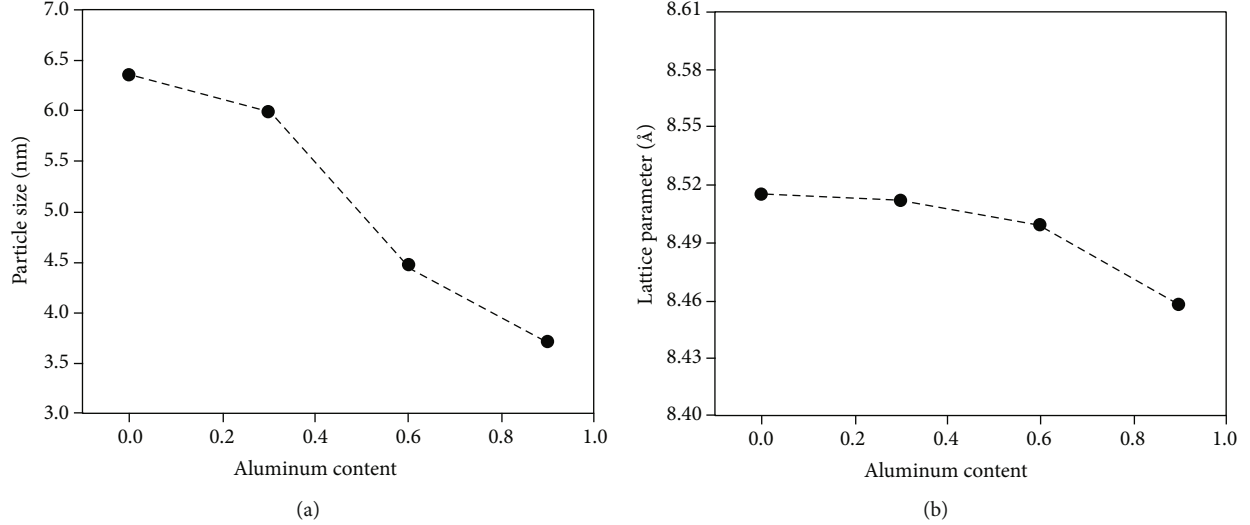


FIGURE 3: Left and right panel presents alteration in the particle size and lattice parameter with the Al content ( $x$ ) in manganese ferrite.

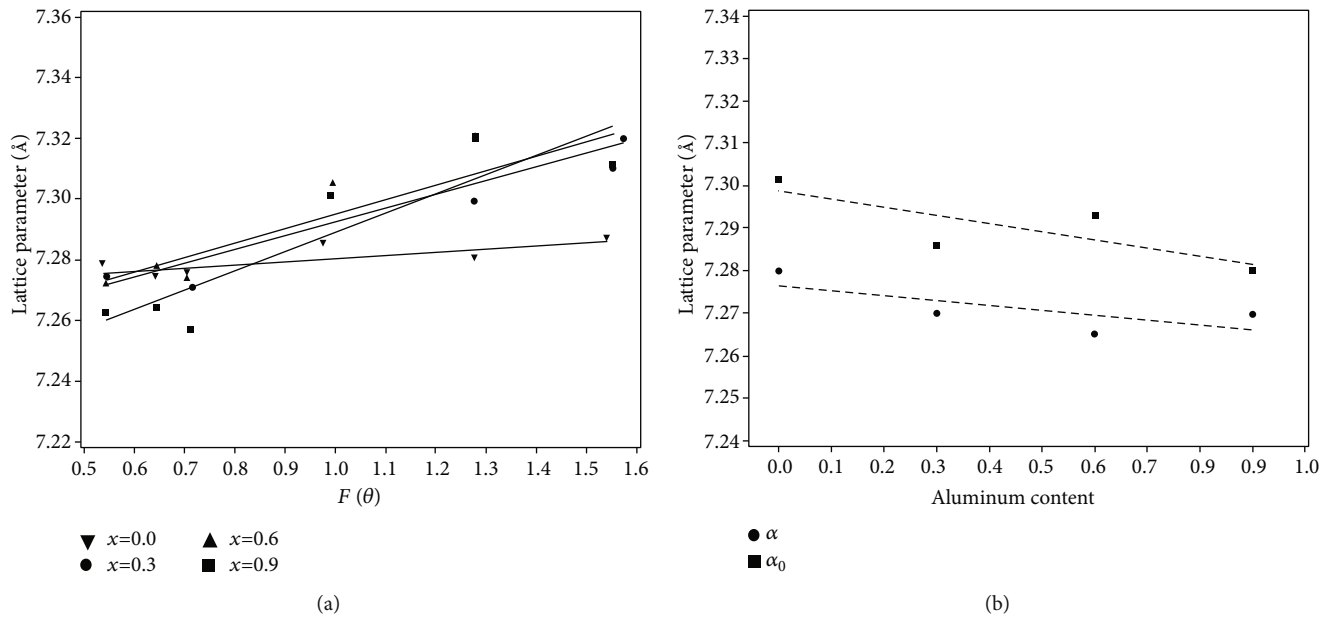


FIGURE 4: (a) The Nelson-Riley representation for  $\text{MnFe}_{2-x}\text{Al}_x\text{O}_4$  and (b) the interactions of the theoretical and experimental lattice constants for  $\text{MnFe}_{2-x}\text{Al}_x\text{O}_4$  ( $x = 0.0, 0.3, 0.6$ , and  $0.9$ ).

The absence of PVP creates aggregation of particles owing to high energy of small particles as reported in the Ostwald ripening process [45]. Table 1 confirms the variation in lattice parameter, X-ray density, bulk density, cell volume, and porosity as the content of nonmagnetic Al changes. Furthermore, increasing Al concentration decreases lattice constant parameters, density, and particle size as shown in Figure 3. Dessai et al. also observed that increasing nonmagnetic  $\text{Al}^{3+}$  content in manganese ferrite decreases lattice parameter and density [46].

The Nelson-Riley function  $F(\theta)$  for each reflection of  $\text{MnFe}_{2-x}\text{Al}_x\text{O}_4$  was calculated by using the following rela-

tion:

$$F(\theta) = \frac{1}{2} \left( \frac{\cos^2 \theta}{\sin \theta} + \frac{\cos^2 \theta}{\theta} \right). \quad (2)$$

Figure 4(a) shows Nelson-Riley function of nanocrystalline  $\text{MnFe}_{2-x}\text{Al}_x\text{O}_4$ . Diffraction angle from  $10$  to  $80^\circ$  was utilized to determine lattice parameters " $a_o$ " by extrapolating  $F(\theta)$ . True lattice value " $a_o$ " and average value " $a$ " variation is shown in Figure 4(b). It is visible from Figure 4(b) that little disparity between true value lattice constant " $a_o$ " and the

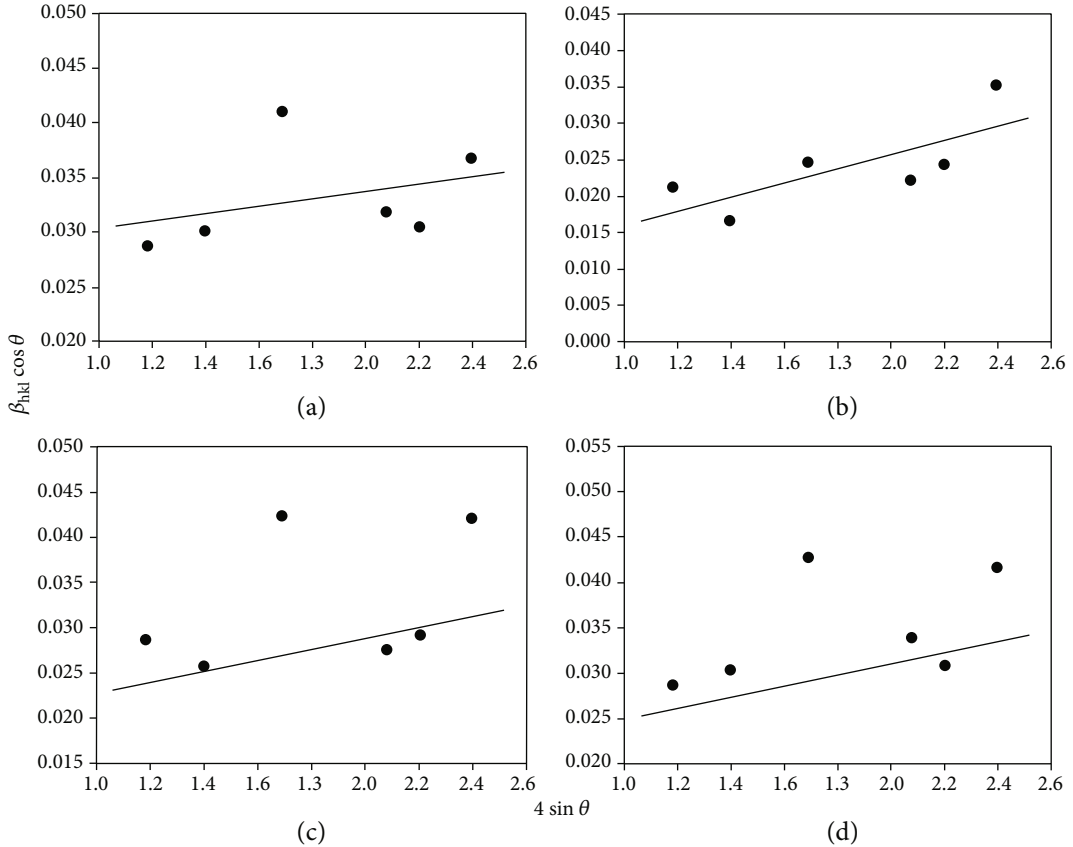


FIGURE 5: Profile of “ $\beta_{hkl}\cos\theta$ ” vs “ $4\sin\theta$ ” of  $MnFe_{2-x}Al_xO_4$  ( $x = 0.0, 0.3, 0.6$ , and  $0.9$ ). (a-d) are associated to diffraction spectrums of different Al concentrations.

average value lattice constant “ $a$ ” existed. Moreover, average value lattice constant “ $a$ ” is slightly more than true value lattice constant “ $a_o$ .” Both true and average value lattice constants reduces as the content of Al elevates. The reduction of both lattice constants may be due to change in ionic radius between  $Al^{3+}$  ( $0.51 \text{ \AA}$ ) and  $Fe^{3+}$  ( $0.67 \text{ \AA}$ ). According to the literature, it is obvious that replacement of highly magnetic  $Fe^{3+}$  ions by nonmagnetic  $Al^{3+}$  reduces lattice constant as Al content elevates [46, 47]. Lattice constant reduces from  $8.515 \text{ \AA}$  to  $8.458 \text{ \AA}$  as the Al content in the doped ferrite increases is shown in Figure 3 (right panel). The reduction in crystallite size from  $6.35 \text{ nm}$  to  $3.71 \text{ nm}$  presented in Figure 3 (left panel) may be due to substitution of larger size  $Fe^{3+}$  ions by smaller size  $Al^{3+}$  ions. High porosity and lattice constant shown in Table 1 are other reasons responsible for crystal size reduction. The parameters  $a$ ,  $V$ ,  $\rho_m$ ,  $\rho_{x-ray}$ , and  $P$  presented in Table 1 were determined from Equations (3) to (7). These parameters decrease as the Al content increases except for porosity which is due to reduction of crystal size and lattice constant. High porosity as the Al content increases may be due to extra vacancies established by substitution of  $Fe^{3+}$  cations by  $Al^{3+}$  cations [48].

$$d = \frac{a}{\sqrt{\frac{2}{h^2 + k^2 + l^2}}}, \quad (3)$$

TABLE 2: Average strain of  $MnFe_{2-x}Al_xO_4$  ( $x = 0.0, 0.3, 0.6$ , and  $0.9$ ).

Sample name	Scherrer method $\langle \varepsilon \rangle \times 10^{-3}$	W-H method $\langle \varepsilon \rangle \times 10^{-3}$
$MnFe_2O_4$	10.90	27.10
$MnFe_{1.7}Al_{0.3}O_4$	7.99	6.50
$MnFe_{1.4}Al_{0.6}O_4$	10.75	21.50
$MnFe_{1.1}Al_{0.9}O_4$	11.44	23.60

$$V = a^3, \quad (4)$$

$$\rho_m = \frac{m}{(\pi r^2)h}, \quad (5)$$

$$\rho_{x-ray} = \frac{ZM}{NV}, \quad (6)$$

$$P = 1 - \frac{\rho_m}{\rho_{x-ray}}. \quad (7)$$

The strain created by crystal defects and distortions is due to addition of Al in manganese ferrites. The average strain  $\langle \varepsilon \rangle$  of Al-doped manganese spinel was calculated

TABLE 3: The bond lengths ( $R_A$  and  $R_B$ ) and hopping lengths for tetrahedral and octahedral sites ( $L_A$  and  $L_B$ ), tetrahedral and octahedral bond lengths ( $d_{AX}$  and  $d_{BX}$ ), the shared tetrahedral edge length ( $d_{AXE}$ ), and shared and unshared octahedral edge lengths ( $d_{BxE}$  and  $d_{BxEU}$ ) of  $MnFe_{2-x}Al_xO_4$  ( $0 \leq x \leq 0.9$ ).

Sample name	Bond length (Å)		Hopping length (Å)		$d_{AX}$ (Å)	$d_{BX}$ (Å)	$d_{AXE}$ (Å)	$d_{BxE}$ (Å)	$d_{BxEU}$ (Å)
	$R_A$	$R_B$	$L_A$	$L_B$					
$MnFe_2O_4$	1.9173	2.0871	2.0870	2.0870	1.9173	2.0870	3.1309	2.8901	3.0118
$MnFe_{1.7}Al_{0.3}O_4$	1.9166	2.0863	2.0863	2.0863	1.9167	2.0863	3.1298	2.8890	3.0107
$MnFe_{1.4}Al_{0.6}O_4$	1.9137	2.0831	2.0831	2.0831	1.9137	2.0831	3.1250	2.8846	3.0061
$MnFe_{1.1}Al_{0.9}O_4$	1.9045	2.0731	2.0731	2.0731	1.9045	2.0730	3.1100	2.8707	2.9916

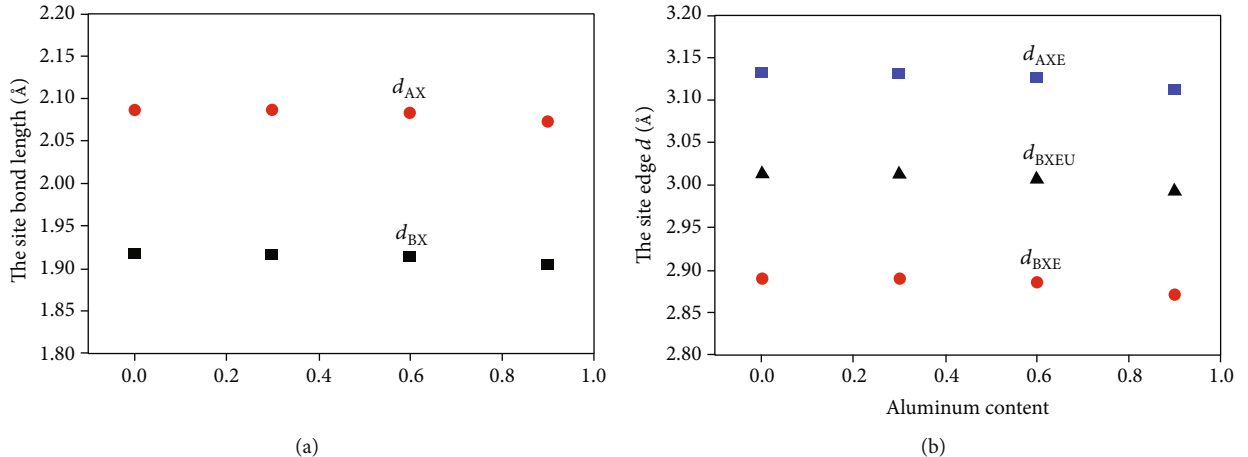


FIGURE 6: (a) The change in the bond lengths ( $d_{AX}$  and  $d_{BX}$ ) and (b) the site edge lengths ( $d_{AXE}$ ,  $d_{BxE}$ , and  $d_{BxEU}$ ) of  $MnFe_{2-x}Al_xO_4$  ( $0 \leq x \leq 0.9$ ).

by employing the following equation:

$$\langle \varepsilon \rangle = \frac{\beta_{hkl}}{4 \tan \theta}. \quad (8)$$

Addition of Equations (1) and (8) produces noticed line breadth in the form of Equation (9).

$$\beta_{hkl} = \frac{k \lambda}{D \cos \theta} + 4 \langle \varepsilon \rangle \tan \theta, \quad (9)$$

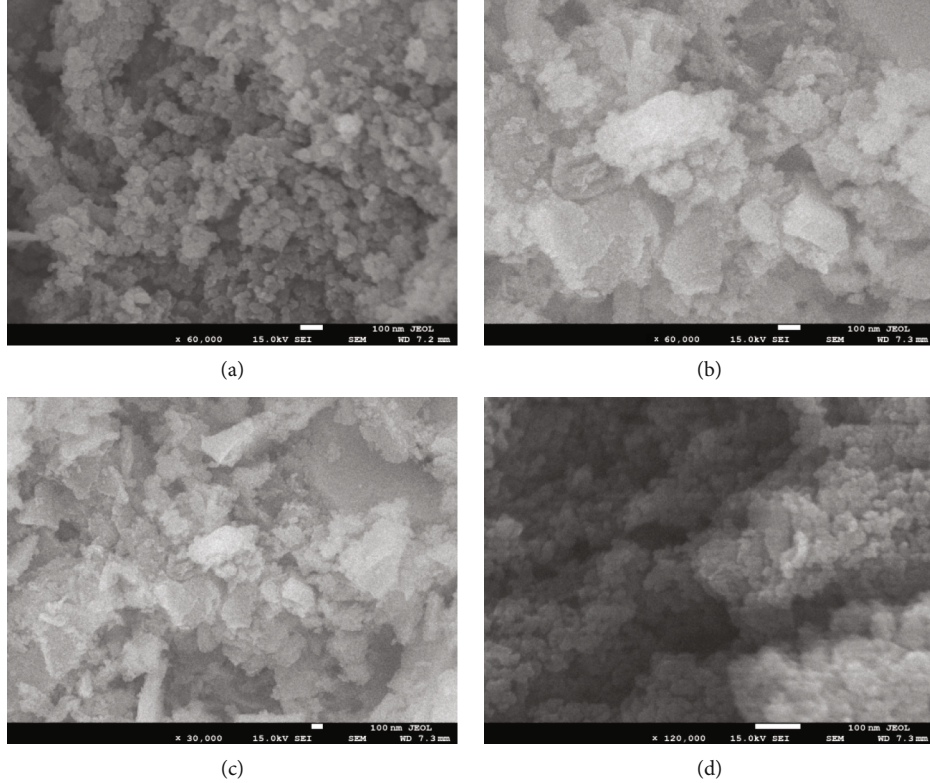
$$\beta_{hkl} \cos \theta = \frac{k \lambda}{D} + 4 \langle \varepsilon \rangle \sin \theta. \quad (10)$$

Williamson-Hall (W-H) calculations shown above in the form of Equations (9) and (10) were used to calculate crystallite size and average strain. The “ $\beta_{hkl} \cos \theta$ ” versus “ $4 \sin \theta$ ” presented in Figure 5 is employed to calculate both the particle size and the strain. The linear fit of the crystal size and strain follows the uniform deformation process, where the strain is assumed as homogeneous in all directions, a property of isotropy. The W-H and Scherer formulas used for the calculation of the average strain were in complete harmony with each other as shown in Table 2.

The bond length of tetrahedral and octahedral sites was affected by the lattice constants which were created by crystal size reduction. The bond lengths shown in Table 3, asso-

ciated to tetrahedral ( $R_A$ ) and octahedral bonding sites ( $R_B$ ) were determined by Equations (11) and (12), where  $\delta = u - 0.375$ . The  $R_A$  and  $R_B$  site is the closest gap between A and B with oxygen ions. The higher  $R_B$  compared to  $R_A$  is the main reason that the  $Mn^{2+}$  cation capability is towards  $O^{2-}$  anions. The existence of  $Al^{3+}$  cations in ferrites reinforces the gap between  $Fe^{3+}$  and  $Al^{3+}$  cations. The  $L_A$  and  $L_B$  values shown in Table 3 determined from Equations (13) and (14) refer to hopping lengths and space between magnetic ions present in the tetrahedral and octahedral bonding sites. The change in hopping lengths of tetrahedral and octahedral sites is associated to change in crystal size which is exactly applicable to lattice constants [49]. The ionic radius alteration between  $Al^{3+}$  (0.51 Å) and  $Fe^{3+}$  (0.67 Å) ions is the other reason associated to change in hopping lengths. The tetrahedral and octahedral bond lengths ( $d_{AX}$  and  $d_{BX}$ ), the shared tetrahedral edge length ( $d_{AXE}$ ), and shared and unshared octahedral edge lengths ( $d_{BxE}$  and  $d_{BxEU}$ ) shown in Table 3 were calculated from Equations (15) to (19). Furthermore, these values shown in Table 3 and Figure 6 suggest reduction as Al content in ferrites increases, therefore indicating complete dominance of the lattice constants and ionic radii [49].

$$R_A = a\sqrt{3} \left( \delta + \frac{1}{8} \right), \quad (11)$$

FIGURE 7: SEM analysis of  $\text{MnFe}_{2-x}\text{Al}_x\text{O}_4$  ( $0 \leq x \leq 0.9$ ).TABLE 4: Comparison of target and actual composition in  $\text{MnFe}_{2-x}\text{Al}_x\text{O}_4$ .

Target composition	Composition by EDX		
	Mn	Fe	Al
$\text{MnFe}_2\text{O}_4$	0.88	2.35	
$\text{MnFe}_{1.7}\text{Al}_{0.3}\text{O}_4$	0.98	2.20	0.42
$\text{MnFe}_{1.4}\text{Al}_{0.6}\text{O}_4$	0.99	1.80	0.71
$\text{MnFe}_{1.1}\text{Al}_{0.9}\text{O}_4$	1.03	1.20	1.06

$$R_B = a \left( 3\delta^2 - \frac{\delta}{2} + \frac{1}{16} \right), \quad (12)$$

$$L_A = 0.25a\sqrt{3}, \quad (13)$$

$$L_B = 0.25a\sqrt{2}, \quad (14)$$

$$d_{Ax} = a\sqrt{3} \left( u - \frac{1}{4} \right), \quad (15)$$

$$d_{Bx} = a \left[ 3u^2 - \left( \frac{11}{4} \right)u + \frac{43}{64} \right]^{1/2}, \quad (16)$$

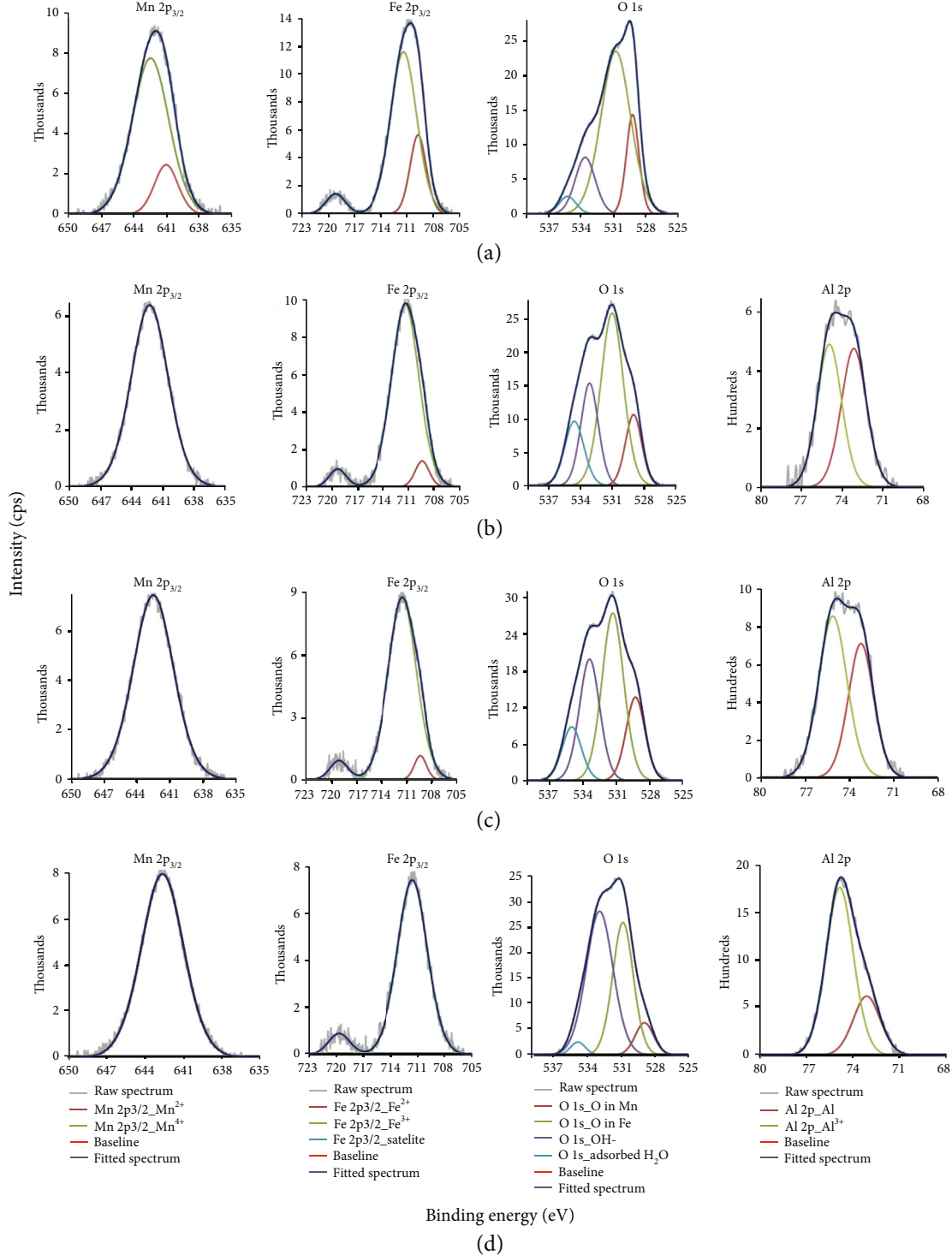
$$d_{AxE} = a\sqrt{2} \left( 2u - \frac{1}{2} \right), \quad (17)$$

$$d_{BxE} = a\sqrt{2}(1 - 2u), \quad (18)$$

$$d_{BxEU} = a \left[ 4u^2 - 3u + \frac{11}{16} \right]^{1/2}. \quad (19)$$

The nanostructure characterization of  $\text{MnFe}_{2-x}\text{Al}_x\text{O}_4$  performed by SEM is presented in Figure 7, where (a) corresponds to pure ferrite and (b-d) correlate to Al-doped manganese ferrites. The scale bar for all the samples is 100 nm. The agglomeration of smaller particles is visible in the nanostructured samples of ferrites. The EDX and elemental investigation averaged over different parts of the samples are presented in Table 4.

The XPS measurements shown in Figure 8 were performed to estimate functionalization of ferrite surface with different active groups. Various chemical states A and B associated with ferrite surface states are presented in Figures 8(a)-8(d). The strong peaks existed in the ferrite spectrum of  $\text{MnFe}_{2-x}\text{Al}_x\text{O}_4$  ( $x = 0.0, 0.3, 0.6$ , and  $0.9$ ) are correlated to Fe, Mn, O, and Al, respectively. The intense signal was adapted to different peaks including Mn 2p, doublet Fe 2p, O 1s, and Al 2p. The Mn 2p is a singlet based at a binding energy (BE) of 641.94 eV. The doublet signal of Mn 2p<sub>3/2</sub> Mn<sup>2+</sup> octa and Mn 2p<sub>3/2</sub> Mn<sup>4+</sup> tetra based at BE of 640.89 eV and 642.43 eV are related to Mn 2p<sub>3/2</sub> peak. Similarly, the same trend was detected for Al in the doped sample; however, a peak deviation of  $\pm 1$  eV was visible. The doublet peak of Fe 2p was deviated from each other by BE 8.45 eV as a result of spin-orbit coupling. The iron 2p<sub>3/2</sub> signals were adapted into three different segments because of the multiplet splitting process. The prominent peaks located

FIGURE 8: XPS spectra of  $\text{MnFe}_{2-x}\text{Al}_x\text{O}_4$  ( $x = 0.0, 0.3, 0.6$ , and  $0.9$ ).

at BE 709.59 eV and 711.24 eV are related to Fe  $2p_{3/2}$   $\text{Fe}^{2+}$  octa and Fe  $2p_{3/2}$   $\text{Fe}^{3+}$  tetra. The doped samples follow a similar trend with a peak deviation of BE  $\pm 2$  eV. The strong peak located at BE 529.88 eV of O is in a multicomponent segment which belongs to the oxide lattice. The remaining less intense peaks of O is based at BE 529.44 eV, 538.99 eV, 533.74 eV, and 535.69 eV which are related to the oxygen

bond formation with Fe, Mn, OH, and adsorbed  $\text{H}_2\text{O}$ , respectively. A similar trend for the oxygen peak was also observed in the ferrite doped samples. The Al 2p peak adapted into two prominent peaks located at BE 73.29 and 74.79 eV which are related to octahedral and tetrahedral sites. The Al peak intensity enhances as the Al concentration increases indicating expected substitution of  $\text{Al}^{3+}$  into

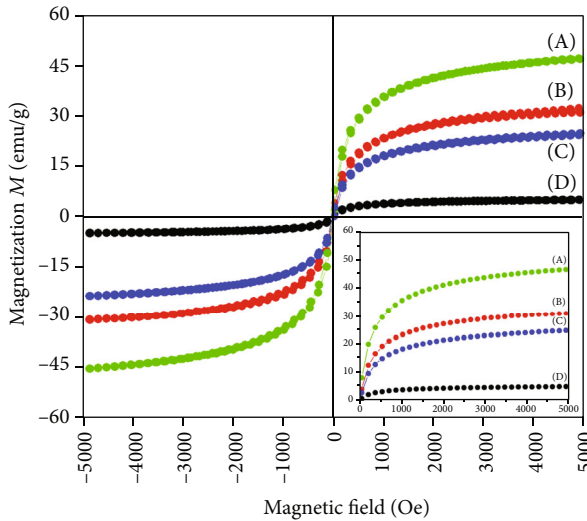


FIGURE 9: Magnetization curves of  $\text{MnFe}_{2-x}\text{Al}_x\text{O}_4$ . The inset profile figure shows saturation magnetization. Profiles (a), (b), (c), and (d) refer to Al concentration of  $x = 0.0, 0.3, 0.6$ , and  $0.9$ , respectively.

TABLE 5: Coercive field ( $H_c$ ), remnant magnetization ( $M_r$ ), saturation magnetization ( $M_s$ ), experimental molar magnetization ( $\eta_{\text{exp}}$ ), and squareness ratio ( $M_r/M_s$ ) determined from hysteresis loops of the ferrite samples.

Sample name	$H_c$ (Oe)	$M_r$ (emu/ g)	$M_s$ (emu/ g)	$\eta_{\text{exp}}$	$R = M_r/M_s$
$\text{MnFe}_2\text{O}_4$	40	5.01	47.32	1.95	0.106
$\text{MnFe}_{1.7}\text{Al}_{0.3}\text{O}_4$	27	1.97	31.90	1.27	0.062
$\text{MnFe}_{1.4}\text{Al}_{0.6}\text{O}_4$	20	1.18	24.71	0.94	0.050
$\text{MnFe}_{1.1}\text{Al}_{0.9}\text{O}_4$	17	0.35	5.02	0.2	0.065

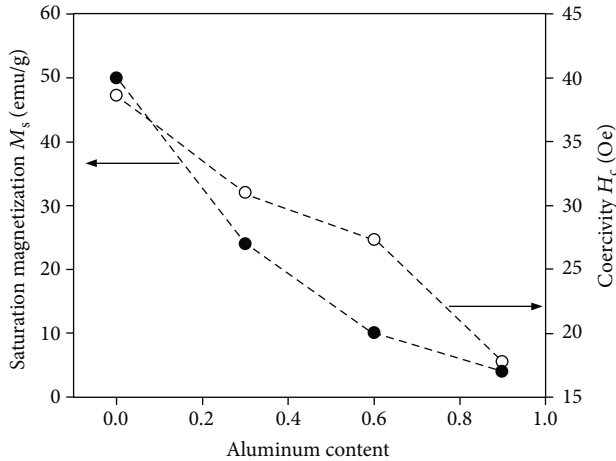


FIGURE 10: Saturation magnetization and coercivity of  $\text{MnFe}_{2-x}\text{Al}_x\text{O}_4$  ( $x = 0.0, 0.3, 0.6$ , and  $0.9$ ).

manganese ferrite. The doping of Al into manganese ferrite responsible for structural and magnetic property variation is the main reason for peak deviation of Mn and Fe in the doped ferrites. The 45%  $\text{Mn}^{2+}$  ions are located at octahedral sites, and 55%  $\text{Mn}^{4+}$  ions are based at tetrahedral sites as far

as unified intensity of the deconvoluted peaks is concerned. The Mn  $2p_{3/2}$  peaks are fitted into two intense peaks located at BE 640.89 eV and 642.43 eV. Moreover, the assessment of  $\text{Fe}^{2+}$  and  $\text{Fe}^{3+}$  based at BE 709.59 eV and 711.24 eV is 78% at the octahedral and 22% at tetrahedral bonding sites [50–52]. The substitution formula of  $\text{MnFe}_{2-x}\text{Al}_x\text{O}_4$  ( $x = 0.0$ ) could be declared as follows:

$$(\text{Mn}_{0.55}^{4+} \text{Fe}_{0.45}^{3+}) [\text{Mn}_{0.45}^{2+} \text{Fe}_{1.55}^{3+}] . \quad (20)$$

Similarly, the distribution of  $\text{Mn}^{2+}$ ,  $\text{Mn}^{4+}$ ,  $\text{Fe}^{2+}$ ,  $\text{Fe}^{3+}$ , and  $\text{Al}^{3+}$  cations at the octahedral and tetrahedral was determined as reported by integrated intensity of deconvoluted strong peaks in  $\text{MnFe}_{2-x}\text{Al}_x\text{O}_4$  ( $x = 0.3, 0.6$ , and  $0.9$ ). The substitution formula of Al-doped manganese ferrite could be designated as follows:

$$\begin{aligned} & (\text{Mn}_{0.55}^{4+} \text{Fe}_{0.47}^{3+} \text{Al}_{0.08}^{3+}) [\text{Mn}_{0.45}^{2+} \text{Fe}_{1.47}^{2+} \text{Al}_{0.08}^{3+}], \\ & (\text{Mn}_{0.55}^{4+} \text{Fe}_{0.39}^{3+} \text{Al}_{0.16}^{3+}) [\text{Mn}_{0.45}^{2+} \text{Fe}_{1.43}^{2+} \text{Al}_{0.12}^{3+}], \\ & (\text{Mn}_{0.55}^{4+} \text{Fe}_{0.19}^{3+} \text{Al}_{0.36}^{3+}) [\text{Mn}_{0.45}^{4+} \text{Fe}_{1.43}^{2+} \text{Al}_{0.12}^{3+}]. \end{aligned} \quad (21)$$

With regard to the assessment of cations among octahedral and tetrahedral,  $\text{Al}^{3+}$  cations choose tetrahedral sites, which deals with chances that  $\text{Al}^{3+}$  cations would substitute  $\text{Fe}^{3+}$  cations. The substitution of  $\text{Fe}^{3+}$  cations by  $\text{Al}^{3+}$  cations is in good compliance with preparation, XRD calculation analysis, EDX spectrum analysis, and magnetic characteristics.

Magnetic hysteresis loops of  $\text{MnFe}_{2-x}\text{Al}_x\text{O}_4$  measured by vibrating sample magnetometer (VSM) at RT are presented in Figure 9. The pristine manganese ferrite sample displays ferromagnetic type nature bearing saturation magnetization of 47.32 emu/g when compared to the Al-doped sample (inset of Figure 9). The representative magnetic characteristics of purified and Al-doped ferrite samples calculated on the basis of the hysteresis loop including  $H_c$ ,  $M_r$ ,  $M_s$ ,  $\eta_{\text{exp}}$ , and  $M_r/M_s$ -squareness ratio are shown in Table 5. The magnetization evaluation was performed by using an additional field area of the calculated  $M(H)$  data by employing Langevin dependence [53]:

$$M(H) = M_s \cdot \left( 1 - \frac{k_B T}{M_s \rho V_{\text{eff}} \mu_o H} \right), \quad (22)$$

where  $V_{\text{eff}}$ ,  $\rho$ , and  $T$  are the effective values of the volume, density, and temperature, respectively, and the other values are related to their typical definitions.

The  $\text{Fe}^{2+}$  and  $\text{Fe}^{3+}$  cation saturation magnetization and coercivity are changed by embedding  $\text{Al}^{3+}$  cations into manganese ferrite. As a result of integrated intensity of deconvoluted peaks, visible saturation magnetization and coercivity addition to  $\text{Mn}^{2+}$  and  $\text{Mn}^{4+}$  ions were negligibly afflicted by the doping of  $\text{Al}^{3+}$  cations into manganese ferrite. The moderate saturation magnetization contraction and coercivity escalation as the Al content is elevated is shown in Figure 10. The decreased value of  $M_s$  and  $M_r$  of the doped ferrite sample may be associated to reduced particle size. The reduction in

$M_s$  after addition of nonmagnetic  $\text{Al}^{3+}$  in ferrite is also confirmed by the literature date reported by Dessai et al. [46]. Furthermore, there is a decrease in the average crystallite size control existence of spin inclination and spin canting, which appear by virtue of a defined size and surface-related effects. The reduction in  $M_s$  and  $M_r$  of doped samples as the Al content is elevated may be due to cation diffusion among the host and embedded groups. The substitution of  $\text{Fe}^{2+}$  and  $\text{Fe}^{3+}$  ions by  $\text{Al}^{3+}$  ions at the octahedral and tetrahedral decreases the bond stability of  $\text{Fe}^{3+}\text{-O-Fe}^{3+}$ . The decrease in the amount of  $\text{Fe}^{2+}$  and  $\text{Fe}^{3+}$  cations in the A- and B-sites decreases the magnetic dipole moment of the B-sublattice and consequently decreases the magnetic moment of ferrites. The exchange of  $\text{Fe}^{3+}$  cations bearing magnetic moment  $5\ \mu_B$  with nonmagnetic  $\text{Al}^{3+}$  cations carrying magnetic moment  $0\ \mu_B$  decreases the superexchange bonding that balances adjacent magnetic dipoles in an antiparallel form. Moreover, the decrease in overall magnetization is possible because of reinforced spin noncollinearity. The elevation of  $\text{Al}^{3+}$  ions which decreases the lattice parameter is due to smaller ionic radius ( $0.55\ \text{\AA}$ ) of  $\text{Al}^{3+}$  cations as compared to  $\text{Fe}^{3+}$  cations ( $0.67\ \text{\AA}$ ). The decrease in magnetization in embedded ferrite is also associated with exchange of cations in the A- and B-sites. The fact is that  $M_s$  builds upon the number and type of cation based at different sites in tetrahedral and octahedral bonding sites in the ferrite. The exchange influences the magnetization  $M_A$  and  $M_B$  of the A and B ferrite sublattices. The affiliation of  $M_B - M_A$  produces magnetization in spinel ferrites. In manganese-based ferrite,  $\text{Mn}^{4+}$  ions choose tetrahedral sites and are emphasized as the Al concentration is elevated. The  $\text{Mn}^{2+}$  ion location in the octahedral sites fades away as the Al content increases. Generally, tetrahedral and octahedral sites in ferrites engaged by  $\text{Fe}^{3+}$  cations are partially substituted by  $\text{Al}^{3+}$  cations. The substitution of  $\text{Fe}^{3+}$  by  $\text{Al}^{3+}$  cations in the B-sites decides magnetization of manganese ferrites. The reduction of magnetization of the Al-doped ferrite samples is due to substitution of  $\text{Al}^{3+}$  ions. The squareness ratio ( $R$ ) less than 0.5 indicates a multidomain structure of ferrite materials while greater than 0.5 signifies a single-domain structure of manganese ferrite. According to the recent investigation carried out related to squareness ratio ( $R$ ) revealed in several places in the literature, the squareness ratio ( $R$ ) observed between 0.01 and 0.1 suggests a multidomain structure of ferrite materials [54–56].

## 4. Conclusions

The significance of  $\text{Al}^{3+}$  cations as a dopant in nanocrystalline manganese ferrite prepared through the thermal treatment method was discussed. The nanostructured samples were characterized by different methods to examine nanocrystallinity, thermal stability, chemical stability, distribution, and morphological properties. The representative Scherrer formula and Williamson-Hall extrapolation equations were employed to determine the crystallite size and lattice strain parameters. The parameters including ionic radii of tetrahedral and octahedral bonding sites, oxygen positional constants, hopping and bond lengths, bond angles and sites, and edge lengths were determined from the XRD

spectrum. The characterization such as XPS and M-H analysis explains the inconsistency in the theoretically anticipated bond angles which implied beefing up of the A-B superexchange synergy. Distribution, chemical form, and degree of inversion were determined from the XPS spectrum. The characteristic magnetic hysteresis loop attained from VSM at RT displays that both  $M_r$  and  $M_s$  are reduced as the Al content is elevated. This contraction was associated with spin noncollinearity and delicate interactions between sublattices.

## Data Availability

The data used to support the findings of this study are included within the article.

## Conflicts of Interest

The authors declare that they have no conflicts of interest.

## Acknowledgments

This project was funded by the Deanship of Scientific Research (DSR) at King Abdulaziz University, Jeddah, under grant no. (G: 191-135-1442). The authors, therefore, acknowledge with thanks the DSR for the technical and financial support.

## References

- [1] R. Valenzuela, "Novel applications of ferrites," *Physics Research International*, vol. 2012, Article ID 591839, 9 pages, 2012.
- [2] M. Latorre-Esteves, A. Cortés, M. Torres-Lugo, and C. Rinaldi, "Synthesis and characterization of carboxymethyl dextran-coated Mn/Zn ferrite for biomedical applications," *Journal of Magnetism and Magnetic Materials*, vol. 321, no. 19, pp. 3061–3066, 2009.
- [3] A. Nigam and S. J. Pawar, "Structural, magnetic, and antimicrobial properties of zinc doped magnesium ferrite for drug delivery applications," *Ceramics International*, vol. 46, no. 4, pp. 4058–4064, 2020.
- [4] K. K. Kefeni, T. A. M. Msagati, T. T. I. Nkambule, and B. B. Mamba, "Spinel ferrite nanoparticles and nanocomposites for biomedical applications and their toxicity," *Materials Science and Engineering: C*, vol. 107, article 110314, 2020.
- [5] X. Wang, L. Gong, D. Zhang, X. Fan, Y. Jin, and L. Guo, "Room temperature ammonia gas sensor based on polyani-line/copper ferrite binary nanocomposites," *Sensors and Actuators B: Chemical*, vol. 322, article 128615, 2020.
- [6] G. Sukmarani, R. Kusumaningrum, A. Noviyanto et al., "Synthesis of manganese ferrite from manganese ore prepared by mechanical milling and its application as an inorganic heat-resistant pigment," *Journal of Materials Research and Technology*, vol. 9, no. 4, pp. 8497–8506, 2020.
- [7] G. Ott, J. Wrba, and R. Lucke, "Recent developments of Mn-Zn ferrites for high permeability applications," *Journal of Magnetism and Magnetic Materials*, vol. 254-255, pp. 535–537, 2003.
- [8] V. Kumar Chakradhary and M. J. Akhtar, "Absorption properties of CNF mixed cobalt nickel ferrite nanocomposite for

- radar and stealth applications," *Journal of Magnetism and Magnetic Materials*, vol. 525, article 167592, 2021.
- [9] M. Hernandez, M. Messagie, O. Hegazy, L. Marengo, O. Winter, and J. van Mierlo, "Environmental impact of traction electric motors for electric vehicles applications," *JLCA*, vol. 22, no. 1, pp. 54–65, 2017.
  - [10] C. C. Agrafiotis and V. T. Zaspalis, "Self-propagating high-temperature synthesis of MnZn-ferrites for inductor applications," *Journal of Magnetism and Magnetic Materials*, vol. 283, no. 2-3, pp. 364–374, 2004.
  - [11] O. Caltun, I. Dumitru, M. Feder, N. Lupu, and H. Chiriac, "Substituted cobalt ferrites for sensors applications," *Journal of Magnetism and Magnetic Materials*, vol. 320, no. 20, pp. e869–e873, 2008.
  - [12] R. Ranga, A. Kumar, P. Kumari, P. Singh, V. Madaan, and K. Kumar, "Ferrite application as an electrochemical sensor: a review," *Materials Characterization*, vol. 178, article 111269, 2021.
  - [13] F. Javed, M. A. Abbas, M. I. Asad et al., "Gd<sup>3+</sup> doped CoFe<sub>2</sub>O<sub>4</sub> nanoparticles for targeted drug delivery and magnetic resonance imaging," *Magnetochemistry*, vol. 7, no. 4, p. 47, 2021.
  - [14] N. Adeela, K. Maaz, U. Khan et al., "Influence of manganese substitution on structural and magnetic properties of CoFe<sub>2</sub>O<sub>4</sub> nanoparticles," *Journal of Alloys and Compounds*, vol. 639, pp. 533–540, 2015.
  - [15] F. Nekvapil, A. Bunge, T. Radu, S. Cinta Pinzaru, and R. Turcu, "Raman spectra tell us so much more: Raman features and saturation magnetization for efficient analysis of manganese zinc ferrite nanoparticles," *Journal of Raman Spectroscopy*, vol. 51, no. 6, pp. 959–968, 2020.
  - [16] M. E. Fleet, "The structure of magnetite: symmetry of cubic spinels," *Journal of Solid State Chemistry*, vol. 62, no. 1, pp. 75–82, 1986.
  - [17] S. K. Pradhan, S. Bid, M. Gateshki, and V. Petkov, "Microstructure characterization and cation distribution of nanocrystalline magnesium ferrite prepared by ball milling," *Materials Chemistry and Physics*, vol. 93, no. 1, pp. 224–230, 2005.
  - [18] P. Puspitasari, U. A. Rizkia, S. Sukarni, A. A. Permanasari, A. Taufiq, and A. B. N. R. Putra, "Effects of various sintering conditions on the structural and magnetic properties of zinc ferrite (ZnFe<sub>2</sub>O<sub>4</sub>)," *Materials Research*, vol. 24, no. 1, pp. 1–5, 2020.
  - [19] B. J. Rani, M. Ravina, B. Saravanakumar et al., "Ferrimagnetism in cobalt ferrite (CoFe<sub>2</sub>O<sub>4</sub>) nanoparticles," *Nano-Structures and Nano-Objects*, vol. 14, pp. 84–91, 2018.
  - [20] Y. W. Ju, J. H. Park, H. R. Jung, S. J. Cho, and W. J. Lee, "Electrospun MnFe<sub>2</sub>O<sub>4</sub> nanofibers: preparation and morphology," *Composites Science and Technology*, vol. 68, no. 7-8, pp. 1704–1709, 2008.
  - [21] Y. Slimani, M. A. Almessiere, M. Sertkol et al., "Structural, magnetic, optical properties and cation distribution of nano-sized Ni<sub>0.3</sub>Cu<sub>0.3</sub>Zn<sub>0.4</sub>Tm<sub>x</sub>Fe<sub>2-x</sub>O<sub>4</sub> (0.0 ≤ x ≤ 0.10) spinel ferrites synthesized by ultrasound irradiation," *Ultrasonics Sonochemistry*, vol. 57, pp. 203–211, 2019.
  - [22] A. Hossain, M. S. I. Sarker, M. K. R. Khan, and M. M. Rahman, "Spin effect on electronic, magnetic and optical properties of spinel CoFe<sub>2</sub>O<sub>4</sub>: a DFT study," *Materials Science and Engineering: B*, vol. 253, article 114496, 2020.
  - [23] T. Ramaprasad, R. Jeevan Kumar, U. Naresh, M. Prakash, D. Kothandan, and K. Chandra Babu Naidu, "Effect of pH value on structural and magnetic properties of CuFe<sub>2</sub>O<sub>4</sub>nano-particles synthesized by low temperature hydrothermal technique," *Materials Research Express*, vol. 5, no. 9, article 095025, 2018.
  - [24] E. E. Ateia, A. A. el-Bassuony, G. Abdelatif, and F. S. Soliman, "Novelty characterization and enhancement of magnetic properties of Co and Cu nanoferrites," *Journal of Materials Science: Materials in Electronics*, vol. 28, no. 1, pp. 241–249, 2017.
  - [25] Z. Zhang, G. Yao, X. Zhang, J. Ma, and H. Lin, "Synthesis and characterization of nickel ferrite nanoparticles via planetary ball milling assisted solid-state reaction," *Ceramics International*, vol. 41, no. 3, pp. 4523–4530, 2015.
  - [26] J. Wang, F. Ren, R. Yi, A. Yan, G. Qiu, and X. Liu, "Solvothermal synthesis and magnetic properties of size-controlled nickel ferrite nanoparticles," *Journal of Alloys and Compounds*, vol. 479, no. 1-2, pp. 791–796, 2009.
  - [27] I. H. Gul, W. Ahmed, and A. Maqsood, "Electrical and magnetic characterization of nanocrystalline Ni-Zn ferrite synthesis by co-precipitation route," *Journal of Magnetism and Magnetic Materials*, vol. 320, no. 3-4, pp. 270–275, 2008.
  - [28] D. H. Chen and X. R. He, "Synthesis of nickel ferrite nanoparticles by sol-gel method," *Materials Research Bulletin*, vol. 36, no. 7-8, pp. 1369–1377, 2001.
  - [29] G. Singh and S. Chandra, "Electrochemical performance of MnFe<sub>2</sub>O<sub>4</sub> nano-ferrites synthesized using thermal decomposition method," *International Journal of Hydrogen Energy*, vol. 43, no. 8, pp. 4058–4066, 2018.
  - [30] J. Huo and M. Wei, "Characterization and magnetic properties of nanocrystalline nickel ferrite synthesized by hydrothermal method," *Materials Letters*, vol. 63, no. 13-14, pp. 1183–1184, 2009.
  - [31] V. Pillai, P. Kumar, M. S. Multani, and D. O. Shah, "Structure and magnetic properties of nanoparticles of barium ferrite synthesized using microemulsion processing," *Colloids and Surfaces: Physicochemical and Engineering Aspects*, vol. 80, no. 1, pp. 69–75, 1993.
  - [32] E. Mazario, P. Herrasti, M. P. Morales, and N. Menéndez, "Synthesis and characterization of CoFe<sub>2</sub>O<sub>4</sub> ferrite nanoparticles obtained by an electrochemical method," *Nanotechnology*, vol. 23, no. 35, article 355708, 2012.
  - [33] R. Nawathey-Dikshit, S. R. Shinde, S. B. Ogale, S. D. Kulkarni, S. R. Sainkar, and S. K. Date, "Synthesis of single domain strontium ferrite powder by pulsed laser ablation," *Applied Physics Letters*, vol. 68, no. 24, pp. 3491–3493, 1996.
  - [34] M. G. Naseri, M. K. Halimah, A. Dehzangi, A. Kamalianfar, E. B. Saion, and B. Y. Majlis, "A comprehensive overview on the structure and comparison of magnetic properties of nanocrystalline synthesized by a thermal treatment method," *Journal of Physics and Chemistry of Solids*, vol. 75, no. 3, pp. 315–327, 2014.
  - [35] M. Naseri, "Optical and magnetic properties of monophasic cadmium ferrite (CdFe<sub>2</sub>O<sub>4</sub>) nanostructure prepared by thermal treatment method," *Journal of Magnetism and Magnetic Materials*, vol. 392, pp. 107–113, 2015.
  - [36] M. G. Naseri, E. B. Saion, M. Hashim, A. H. Shaari, and H. A. Ahangar, "Synthesis and characterization of zinc ferrite nanoparticles by a thermal treatment method," *Solid State Communications*, vol. 151, no. 14–15, pp. 1031–1035, 2011.
  - [37] S. Gyergyek, D. Makovec, A. Kodre, I. Arčon, M. Jagodić, and M. Drofenik, "Influence of synthesis method on structural and magnetic properties of cobalt ferrite nanoparticles," *Journal of Nanoparticle Research*, vol. 12, no. 4, pp. 1263–1273, 2010.

- [38] S. Jauhar, J. Kaur, A. Goyal, and S. Singhal, "Tuning the properties of cobalt ferrite: a road towards diverse applications," *RSC Advances*, vol. 6, no. 100, pp. 97694–97719, 2016.
- [39] K. Chakrapani, G. Bendt, H. Hajiyani et al., "Role of composition and size of cobalt ferrite nanocrystals in the oxygen evolution reaction," *ChemCatChem*, vol. 9, no. 15, pp. 2988–2995, 2017.
- [40] S. Prathapani, M. Vinitha, T. V. Jayaraman, and D. Das, "Effect of Er doping on the structural and magnetic properties of cobalt-ferrite," *Journal of Applied Physics*, vol. 115, no. 17, pp. A7A502–A7A5023, 2014.
- [41] S. K. Pendyala, K. Thyagarajan, A. GuruSampath Kumar, and L. Obulapathi, "Effect of Mg doping on physical properties of Zn ferrite nanoparticles," *Journal of the Australian Chemical Society*, vol. 54, no. 3, pp. 467–473, 2018.
- [42] F. R. Mariosi, J. Venturini, A. da Cas Viegas, and C. P. Bergmann, "Lanthanum-doped spinel cobalt ferrite ( $\text{CoFe}_2\text{O}_4$ ) nanoparticles for environmental applications," *Ceramics International*, vol. 46, no. 3, pp. 2772–2779, 2020.
- [43] J. A. Paulsen, A. P. Ring, C. C. H. Lo, J. E. Snyder, and D. C. Jiles, "Manganese-substituted cobalt ferrite magnetostrictive materials for magnetic stress sensor applications," *Journal of Applied Physics*, vol. 97, no. 4, article 044502, 2005.
- [44] H. Kaur, A. Singh, V. Kumar, and D. S. Ahlawat, "Structural, thermal and magnetic investigations of cobalt ferrite doped with  $\text{Zn}^{2+}$  and  $\text{Cd}^{2+}$  synthesized by auto combustion method," *Journal of Magnetism and Magnetic Materials*, vol. 474, pp. 505–511, 2019.
- [45] F. Z. Mou, J. G. Guan, Z. G. Sun, X. A. Fan, and G. X. Tong, "In situ generated dense shell-engaged Ostwald ripening: A facile controlled- preparation for  $\text{BaFe}_{12}\text{O}_{19}$  hierarchical hollow fiber arrays," *Journal of Solid State Chemistry*, vol. 183, no. 3, pp. 736–743, 2010.
- [46] P. P. Gauns Dessai, S. S. Meena, and V. M. S. Verenkar, "Influence of addition of  $\text{Al}^{3+}$  on the structural and solid state properties of nanosized Ni-Zn ferrites synthesized using malic acid as a novel fuel," *Journal of Alloys and Compounds*, vol. 842, article 155855, 2020.
- [47] K. V. Kumar, D. Paramesh, and P. V. Reddy, "Effect of Aluminum doping on structural and magnetic properties of Ni-Zn ferrite nanoparticles," *World Journal of Nano Science and Engineering*, vol. 5, no. 3, pp. 68–77, 2015.
- [48] S. P. Waghmare, D. M. Borikar, and K. G. Rewatkar, "Impact of Al doping on structural and magnetic properties of Co-ferrite," *Materials Today*, vol. 4, pp. 11866–11872, 2017.
- [49] S. U. Rather and O. M. Lemine, "Effect of Al doping in zinc ferrite nanoparticles and their structural and magnetic properties," *Journal of Alloys and Compounds*, vol. 812, pp. 152058–152068, 2020.
- [50] G. Kumar, R. K. Kotnala, J. Shah et al., "Cation distribution: a key to ascertain the magnetic interactions in a cobalt substituted Mg–Mn nanoferrite matrix," *Physical Chemistry Chemical Physics*, vol. 19, no. 25, pp. 16669–16680, 2017.
- [51] S. R. Naik and A. V. Salker, "Change in the magnetostructural properties of rare earth doped cobalt ferrites relative to the magnetic anisotropy," *Journal of Materials Chemistry*, vol. 22, no. 6, pp. 2740–2750, 2012.
- [52] R. S. Yadav, I. Kuřítková, J. Vilcakova et al., "Impact of grain size and structural changes on magnetic, dielectric, electrical, impedance and modulus spectroscopic characteristics of  $\text{CoFe}_2\text{O}_4$  nanoparticles synthesized by honey mediated sol-gel combustion method," *Advances in Natural Sciences: Nanoscience*, vol. 8, article 045002, 2017.
- [53] A. T. Raghavender, S. E. Shirath, D. Pajic et al., "Effect of Al doping on the cation distribution in copper ferrite nanoparticles and their structural and magnetic properties," *Journal of the Korean Physical Society*, vol. 61, no. 4, pp. 568–574, 2012.
- [54] S. T. Assar and H. F. Abosheisha, "Effect of Ca substitution on some physical properties of nano-structured and bulk Ni-ferrite samples," *Journal of Magnetism and Magnetic Materials*, vol. 374, pp. 264–272, 2015.
- [55] H. N. Chaudhari, P. N. Dhruv, C. Singh, S. S. Meena, S. Kavita, and R. B. Jotania, "Effect of heating temperature on structural, magnetic, and dielectric properties of magnesium ferrites prepared in the presence of *Solanum lycopersicum* fruit extract," *Journal of Materials Science: Materials in Electronics*, vol. 31, pp. 18445–18463, 2020.
- [56] A. R. Kagdi, N. P. Solanki, F. E. Carvalho et al., "Influence of Mg substitution on structural, magnetic and dielectric properties of X-type barium![single bond](<https://sdfestaticassets-us-east-1.sciedirectassets.com/shared-assets/55/entities/sbnd.gif>)zinc hexaferrites  $\text{Ba}_2\text{Zn}_{2-x}\text{Mg}_x\text{Fe}_{28}\text{O}_{46}$ ," *Journal of Alloys and Compounds*, vol. 741, pp. 377–391, 2018.